Design and Properties of a scanning EMR probe Microscope

S.A. Solin
Center for Materials Innovation And Department of Physics,
Washington University in St. Louis 1 Brookings Drive St. Louis, Missouri, 63130, USA

The design, fabrication, and predicted performance of a new type of magnetic scanning probe microscope based on the newly discovered phenomenon of extraordinary magnetoresistance (EMR) is described. It is shown that the new probe should advance the state of the art of both sensitivity and spatial resolution by an order of magnitude or more.

I. INTRODUCTION

During the past one and one half decades, various types of scanning probes have been developed to both image and measure the spatial variation of the magnetic fields near the surfaces of material systems such as high-density recording media,[1] low and high temperature superconductors[2] and various types of other magnetic[3] and non-magnetic[4] systems. Understanding the microstructural details of the magnetic field distributions produced by such systems is crucial to the elucidation of the basic physical phenomena that govern their behavior. This understanding is greatly facilitated by high-resolution imaging and high sensitivity measurement of the magnetic field distribution associated with each system. The development of magnetic force microscopy (MFM)[5] has greatly contributed to this endeavor but MFM has a few notable drawbacks. It measures the field gradient as opposed to the field itself. This complicates analysis and reduces the accuracy of the field distribution determination. In addition, the self-field of the MFM tip can be quite large, 1000 Gauss, giving rise to an invasive probe in which the magnetic properties of the system under investigation are perturbed by the investigative tool.

To overcome the deficiencies in MFM Oral and coworkers developed a scanning Hall probe microscope (SHPM)[6] based on the GaAs/AlGaAs quantum well heterostructure and employed it to study vortecies in superconductors[7] and the field distribution on or near the surface of insulating ferromagnets.[2] The SHPM is most attractive for low temperature measurements since its field sensitivity is proportional to the square root of the carrier mobility. That mobility can be of order 10^6 cm^2/Vs for GaAs quantum wells at liquid He temperature but drops by a factor of 1000 or more at room temperature.[8] Moreover, the three-dimensional spatial resolution of the SHPM is currently at best about 200 nm 200 nm 25 nm the latter being in the vertical direction. While this spatial resolution is adequate to distinguish key magnetic features (e.g. vortecies) in superconductors of interest and some features of ferromagnetic domains in insulators or metals, it is not sufficient to assess the details of the field distribution of such features without imposing deconvolution techniques that limit the accuracy of such determinations. However, the SHPM has a very short response time and it is constructed from non-magnetic material that is beneficial in minimizing the self-field of the probe.

The discovery of Extraordinary Magnetoresistance (EMR) by Solin and coworkers[9] and the fabrication of nanoscopic EMR field sensors[10] now provide the opportunity to advance the state of the art of semiconductor based scanning magnetic field probes by offering at least an order of magnitude higher sensitivity and an order of magnitude higher spatial resolution over a temperature range from liquid He temperatures to room temperature without sacrificing any of the intrinsic advantages of the SHPM. The route to this state of the art advance is effectively the replacement of the Hall probe in the SHPM with an appropriately designed and developed EMR probe thereby yielding a scanning EMR probe microscope or SEMRPM. Examples of measurements that will be made possible by the SEMRPM include but are not limited to:

- Imaging the bit field in ultra high density (TB/in^2) magnetic recording media
- Ultrahigh resolution studies of current flow in quantum wires
- Fault detection in nanocircuits
- Probing new static and dynamic details of the vortex melting transition and phase diagram of high temperature superconductors

Here we describe the critical design criteria for an SEMRPM and evaluate the optimized performance properties which it can be expected to exhibit.

II. BACKGROUND – EMR PHYSICS, MACRO- AND NANO-STRUCTURES

There are two principal contributions to the magnetoresistance (MR) of any resistive device, namely a physical contribution and a geometric contribution.[11] The physical contribution derives from the dependence of intrinsic material properties such as carrier concentration and carrier mobility on the applied magnetic field. The geometric contribution is an extrinsic property that depends on the shape of the device, the placement and geometry of the (metallic) contacts and, the placement and geometry of any inhomogeneities that may be present.

The geometric contribution to the MR also depends on the intrinsic physical properties of the inhomogeneities relative to those of the host material, e.g. on the conductivity ratio.[12] For most materials of current interest as MR sensors such as layered magnetic metals which exhibit giant MR (GMR)[13] or tunneling MR (TMR)[14] and the magnetic layered oxide manganites which exhibit colossal MR (CMR),[15] the physical contribution to the MR is dominant. However, Solin and his colleagues have recently shown that judiciously designed hybrid structures composed of a non-magnetic narrow-gap semiconductor matrix with high carrier mobility and a non-magnetic metallic inhomogeneity or shunt can exhibit a room temperature MR that is not only dominated by the geometric contribution but also attains room temperature values of order 1,000,000% which is several orders of magnitude higher than what has been achieved with conventional GMR, TMR or CMR devices.[9] The new phenomenon was subsequently dubbed extraordinary MR or EMR.[16] The proof of principal demonstration of EMR was accomplished with symmetric 4-probe macroscopic van der Pauw (vdP) disc structures formed from Te-doped InSb (electron concentration $n = 2 \quad 10^{17}$ cm^{-3} and mobility $= 4.5 \quad 10^{4}$ cm^2/Vs) containing a concentric cylindrical metallic inhomogeneity as depicted in the inset of Fig. 1. Solin et al. also showed that in general, $EMR(H; H_{bias}) = [R^{eff}(H + H_{bias}) - R^{eff}(H_{bias})]/R^{eff}(H_{bias})$ where H is the applied field normal to the plane of the device, $R_{eff}(H)$ is the effective field-dependent resistance measured in a 4-probe configuration, H_{bias} is the bias field and H is the applied or signal field (not the field gradient). For small signals

$$EMR(H \to 0; H_{bias}) = \frac{1}{R^{eff}(H_{bias})} \left.\frac{dR^{eff}(H)}{dH}\right|_{H_{bias}} H \qquad (1)$$

where $[dR^{eff}(H)/dH]_{H_{bias}}$ is the current sensitivity. In the zero bias large signal but still low field limit, $H \ll 1$,

$$EMR(H; 0) = \frac{R^{eff}(H) - R_0^{eff}}{R_0^{eff}} = G_S(H)[\ H\ ]^2 \quad G_{AS}(H)[\ H\ ]: \qquad (2)$$

Here $G_S(H)$ and $G_{AS}(H)$ are, respectively, symmetric and antisymmetric geometric factors which depend on the shape, location and physical properties of the conducting inhomogeneity and contacts while $R^{eff}(0) = R_0^{eff}$. [For the symmetric structure shown in the inset of Fig. 1. $G_{AS}(H) = 0$.] Clearly, narrow-gap high mobility semiconductors such as InSb and InAs are choice materials for EMR devices.

The magnetotransport properties of the macroscopic vdP structure shown in the inset of Fig. 1. can be quantitatively accounted for using the above equations together with both finite element analysis[17] and analytic techniques.[18] However, the EMR phenomenon can be readily understood using a simple though non-intuitive classical physics analysis. The components of the magnetoconductivity tensor $\underline{\sigma}(H)$ for the semiconductor are $\sigma_{xx}(\ ) = \sigma_{yy}(\ ) = \ = 1 + \ ^2$, $\sigma_{zz}(\ ) = \ $, and $\sigma_{xy}(\ ) = \ = 1 + \ ^2 = \ \sigma_{yx}(\ )$ with $= H$ and all others being zero. If the electric field on the vertical surface of the inhomogeneity is $\vec{E} = E_x\hat{x} + E_y\hat{y}$, the current density is $\vec{J} = \underline{\sigma}(H)\vec{E}$. The electric field is everywhere normal to the equipotential surface of a highly conducting inhomogeneity. At $H = 0$, $\underline{\sigma}(H)$ is diagonal so $\vec{J} = \ \vec{E}$ and the current flows into the inhomogeneity which acts as a short circuit. At high H (> 1), the off-diagonal components of $\underline{\sigma}(H)$ dominate so $\vec{J} = (\ = \ )[E_y\hat{x} \quad E_x\hat{y})]$ and $\vec{J} \perp \vec{E}$. Equivalently, the Hall angle between the electric field and the current density approaches 90^0, and the current becomes tangent to, i.e. deflected around, the inhomogeneity. Thus, the inhomogeneity acts as an open circuit. The transition of the inhomogeneity from short circuit at low H to open circuit at high H results in a geometric enhancement of the MR of the semiconductor even if its resistivity (conductivity)

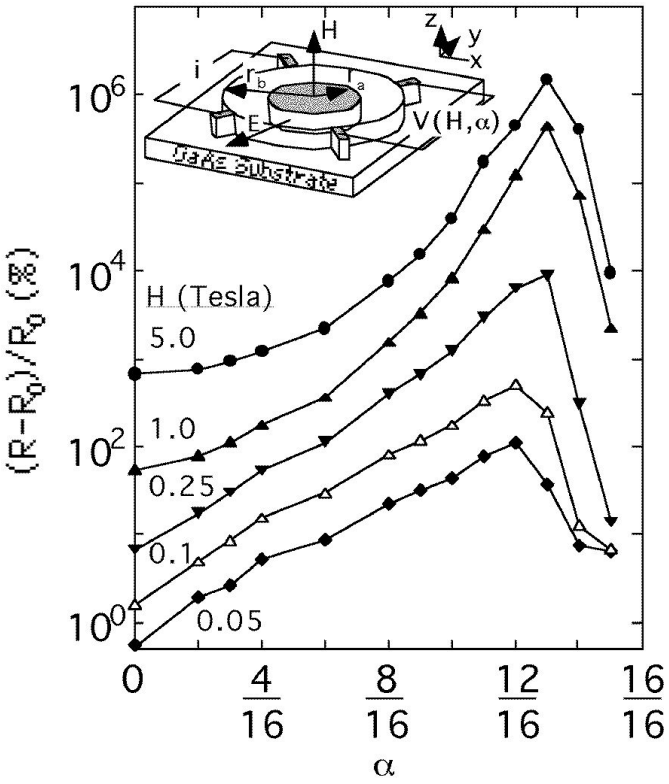

FIG. 1: The field-dependence of the magnetoresistance, $(R - R_0)/R_0$, of a Te-doped InSb van der Pauw disk of radius r_b in which is embedded a concentric right circular cylinder of Au of radius r_a. The filling factor is $= r_a/r_b$. Inset – a schematic diagram of a composite disk with the current and voltage leads configured for the magnetoresistance measurement configuration.

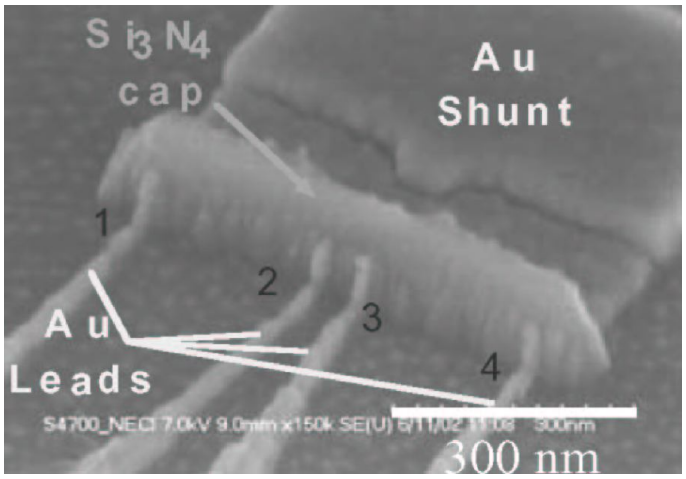

FIG. 2: An electron micrograph of a mesoscopic van der Pauw plate structure formed from an InSb/InAl$_{1-x}$Sb$_x$ quantum well. The current leads, voltage leads and external shunt are labeled as indicated.

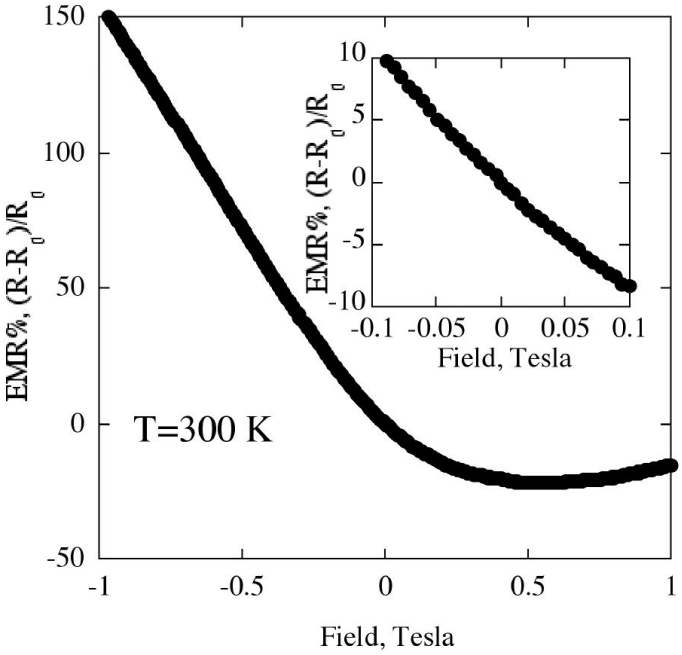

FIG. 3: The field dependence of the magnetoresistance of the mesoscopic van der Pauw plate structure shown in Fig. 2. Bias current density, 5 10^3A/cm^2.

is field-independent (i.e. the physical MR is zero). The MR increases with filling factor, , (see caption, Fig. 1.) because R_0 decreases. However, when becomes sufficiently large so that the low-field current flows mostly through the inhomogeneity, the MR will be that of the inhomogeneity itself, which for Au is negligibly small. Then an appreciable MR is only observed when H is sufficient to deflect the current from the inhomogeneity such that the conductance through the metallic inhomogeneity is smaller than the conductance through the semiconductor annulus of thickness n_b $_4$. Clearly, the EMR effect results from orbital rather the spin degrees-of-freedom of the charge carriers.

Using conformal mapping methods Solin and coworkers showed experimentally and theoretically that macroscopic externally shunted vdP plates were galvanomagnetically equivalent to the internally shunted disc shown in the inset of Fig. 1.[18] They then faced the formidable challenge of scaling such EMR devices to the nanoscopic sizes required for ultra-high spatial resolution and high sensitivity detection of magnetic fields. To meet this challenge, they used an InSb/In$_x$Al$_{1-x}$Sb quantum well structure and state of the art suspended mask e-beam lithography incorporating a new type of resist, calixarine, to fabricate the structure shown in Fig. 2.[16] Details of the fabrication method are provided elsewhere[19] with one exception. The leads and shunt on the device shown in Fig. 2 were insulated from the floor of the mesa containing the quantum-well by an Al_2O_3 layer that extended to within 50 nm of the mesa sidewall.

The field dependence of the room temperature magnetoresistance of the externally shunted nanoscopic EMR device shown in Fig. 2 is shown in Fig. 3. As can be seen, the EMR reaches values as high as 5% at zero bias and a signal field of 0.05 T. To our knowledge, this is the highest room temperature MR level obtained to date for a patterned magnetic sensor with this spatial resolution. Moreover, with a modest bias field of 0.2 T corresponding to the zero-field offset[20] in Fig. 3, the measured EMR is 35% at a signal field of 0.05 T. [The offset is associated with the asymmetric placement of the leads.] Also note that the device can be biased into a field region where the EMR response is linear with field, a feature that can simplify signal amplification. Equally significant is the fact that the current sensitivity, at a magnetic field bias of 0.2 T has a large measured value of 585 /T at room temperature. It is this figure that enters directly into the calculation of the signal to noise ratio as will be discussed below.

III. KEY FACTORS IN THE DESIGN OF AN SEMRPM

A. Probe Materials

Two materials and material systems will be of primary interest for nanoscopic EMR probes, namely InSb and InAs as well as quantum well structures based on those materials. InSb has already been shown to be an effective material for nanoscopic EMR sensors and thus for room temperature SEMRPM applications. But the Schottky barrier associated with the surface depletion layer in InSb[21] will limit its use in low temperature probes because of unacceptable increases in the shunt-mesa sidewall interface resistance. Barrier effects also preclude the use of GaAs/AlGaAs two dimensional elec-

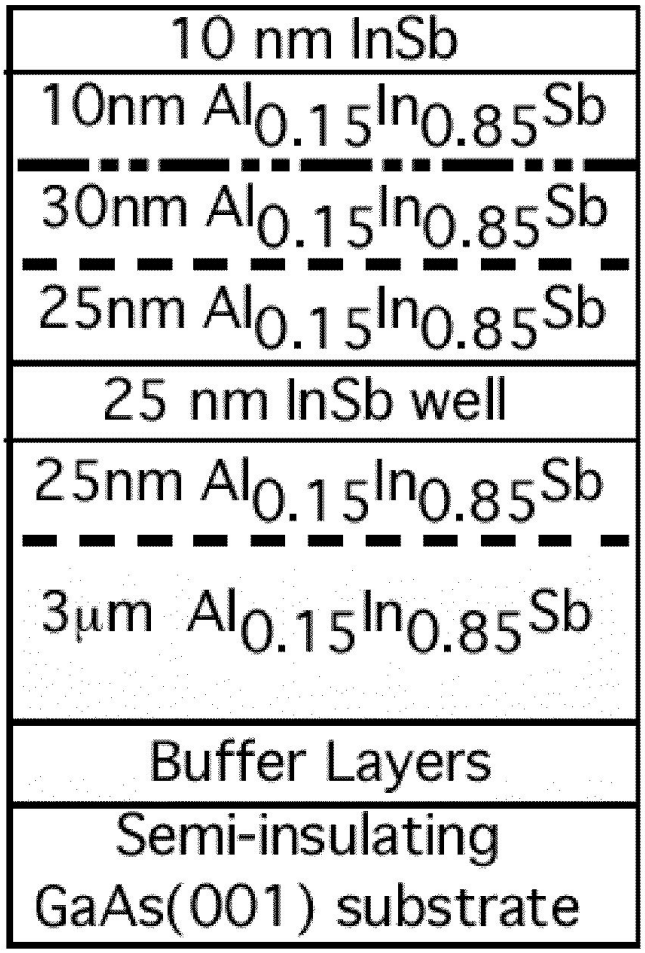

FIG. 4: InSb/AlInSb quantum well structure with high mobility carriers in the InSb well at room temperature. The double (single) dashed line represents a -doped Si layer with 2D concentration 9.5×10^{11} cm^{-2} (2.75×10^{11} cm^{-2}).

tron gas (2Deg) structures, in nanoscopic EMR devices with mesa widths of order 30 nm, notwithstanding their huge mobility at low temperature. The material of choice for low temperature EMR probes will be InAs. It has already been shown to be effective in microscopic low temperature EMR devices.[22] Moreover, InAs has an n-type surface accumulation layer with a high 2D carrier concentration of 1×10^{12} cm^{-2} and reasonable mobility of 2×10^4 cm^2/Vs both of which are relatively temperature independent below 77 K.[23] Therefore, contact resistance to InAs with a number of metals is low even at low temperature.

For a number of applications including the SEMRPM, it is desirable for the EMR sensor to be very thin in the vertical direction so that it has very high spatial resolution (20 nm) in that direction and so that its active region can be positioned very close to the surface of the medium creating the field to be sensed. Unfortunately, although bulk thin film InSb on GaAs substrates can be prepared with room temperature electron mobility of order 50,000 cm^2/Vs, as one reduces the film thickness to values below about 1 m, the mobility of currently available InSb films drops precipitously reaching a value of only 100 cm^2/Vs. at a film thickness of 0.1 m.[24] Therefore, in order to provide the high carrier mobility that is required for high sensitivity at low fields in an EMR device [see Eq. (2)] the InSb mesa shown in Fig. 2 was etched from the InSb/$In_xAl_{1-x}Sb$ quantum well structure shown schematically in Fig. 4. This structure contains a 20 nm thick quantum well located about 90 nm from the top of the Si_3N_4 insulating cap layer [added to prevent shorting between the leads and the shunt.] The 2D concentration and the mobility of carriers in the well were measured to be $n = 2.7 \times 10^{11}$ cm^{-2} and $= 2.3 \times 10^4$ cm^2/Vs at room temperature. Note from Fig. 2 that the longitudinal resolution (along x) of the device is set by the spacing of the voltage probes because the shunt is designed to contact the opposite mesa sidewall along a length equal to the spacing between the voltage probes. Thus the volumetric resolution of the EMR device shown in Fig. 2 is 35 nm (the voltage probe spacing) 30 nm (the width of the mesa) 20 nm (the thickness of the quantum-well) along x, y and z, respectively.

B. Device Geometry and its Impact on Transport and Contact Resistance

The room temperature mean free path of the carriers in an InSb quantum-well is $' = h\sqrt{2n}/(e) = 200$ nm. Thus one would expect the transport in a nanostructure to be ballistic in which case it can be shown that the expected EMR would be at least a factor of 5 lower than what is observed in Fig. 3. However, Solin et al. have suggested that the transport is in-fact still diffusive as a result of the randomization of the carrier velocities due to scattering off of the rough mesa sidewalls[16] (see Fig. 2). The scattering process is enhanced because the roughness wavelength is of the order of the Fermi wavelength of the carriers $_F = \sqrt{2}/n = 48$ nm. Given the assumption of diffusive transport, the EMR of the nanoscopic device though noteworthy, is still about a factor of 20 lower than that obtained with the a macroscopic plate of the same geometry fabricated from thin film Te-doped InSb with a room temperature mobility of 4.5×10^4 cm^2/Vs.[18] Part of this difference is due to the mobility difference thus yielding a reduction in EMR of a factor of $(4.5 \times 10^4/2.3 \times 10^4)^2 = 3.8$. The additional order of magnitude reduction derives from current leakage through the mesa floor (quantum well lower barrier) which carries a much higher proportion of the current than does the quantum well itself.

Rather than rendering the carriers diffusive by scattering off of the striated mesa sidewalls fluted current and voltage leads can be employed as depicted schematically in Fig. 5.

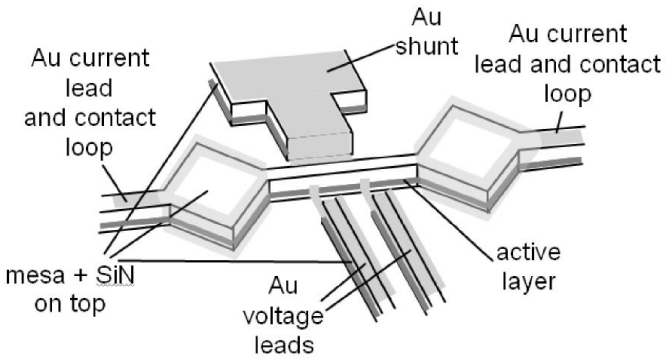

FIG. 5: Schematic diagram of EMR device with fluted current leads. [Features not to scale.]

The current leads will have dimensions much larger than the carrier mean free path. Thus current launched into the region of the shunt and voltage leads will already be diffusive owing to interactions in the fluted regions. Fluted leads will have the additional benefit of increasing the area of the current contacts and reducing contact resistance.

Of more concern is the contact resistance at the shunt interface. This diminishes the effectiveness of the shunt and reduces the EMR. For instance, the specific contact resistance of Au and similar metals with InSb at room temperature[21] is 10^{-7} Ω cm^2 while the contact area of the shunt used in the device shown in Fig. 2. is 9×10^{-12} cm^2. This yields a contact resistance of 1.1×10^{4} Ω that is about a factor of 10 larger than the intrinsic value of R_{out}. Unfortunately, the shunt contact area cannot be increased without diminishing longitudinal resolution nor can the shunt be fluted without sacrificing transverse resolution. Moreover, the usual techniques of diffusing a metal such as In into the contact to eliminate the Schottky barrier or of adding a heavily doped interface layer between the quantum well side wall and the shunt are not applicable to nanoscopic structures of the type addressed here. If the SNR for the InSb – Au system is inadequate for a particular probe application, the solution to the contact problem is to substitute InAs for InSb. This will be discussed below.

C. Bias Electric Field and Maximum Input Current

Three processes may, in principal, limit the maximum bias field one can apply to an EMR sensor. These are joule heating in the metal and/or semiconductor, electromigration in the metal if it is an alloy structure and nonlinear transport in the semiconductor. One can anticipate that nonlinear transport in the semiconductor will occur at bias fields well below those demarking the onset of the other processes (see below). The source of the nonlinear response in narrow-gap semiconductors is the scattering of carriers off of phonons and plasmons when those carriers are accelerated to sufficient energies to interact strongly with those entities.[25] A direct consequence of the scattering by optic phonons is the reduction of the carrier mobility with increasing applied current or electric field. As a result the mobility of both InSb and InAs is essentially field independent (Ohmic) up to critical fields of order $E_c \sim 400$ V/cm above which, the mobility decreases precipitously with increasing field. The field dependence of the mobility of those materials can be well accounted for using a "catchment" model that incorporates the plasmon screening length as a key parameter and is applicable to diffusive transport.[25]

From the information in Fig. 1, we can estimate the current density at which non-linear effects will occur in InSb. The critical current density that defines the onset of non-Ohmic response is given by $J_c = \sigma E_c = ne\mu E_c$ where σ is the material conductivity, n is the carrier density (for electrons, the dominant carriers in InSb) and μ is the carrier mobility. If we assume typical carrier concentration of $n \sim 2 \times 10^{17}$ cm^{-3} and a typical mobility of $\sim 3 \times 10^{4}$ cm^2/Vs, then we find that $J_c \sim 3 \times 10^{5}$ Amps/cm^2. Since critical currents for the onset of heat damage in InSb and InAs are an order of magnitude higher,[25] the onset of nonlinear transport is a primary concern in establishing the maximum signal to noise ratio one can expect to obtain with an EMR sensor constructed from those materials.

D. SEMRPM Performance

The performance of a magnetic sensor is, of course, measured by the signal to noise ratio at the operating conditions under which it will be employed. We will propose sensor designs that result in diffusive transport at all temperatures of interest. For such EMR devices two noise sources are relevant, 1/f noise and thermal or Johnson noise. In this case, if the effective resistance is quadratic with field, e.g. $R^{eff} = R_0^{eff}\left(1 + G^2 (H - H_0)^2\right)$ where H_0 is the zero-field offset, the voltage signal to noise ratio can be written in the following form:[26]

$$SNR(f) = \frac{I_{in}\left(\frac{dR^{eff}}{dH}\right)_{H_{bias}} H}{\left[\left(\frac{V}{L}\right)^2 \left(eR_{out}\frac{f}{\Delta f} + 4kTR_{out}\right)\Delta f\right]^{\frac{1}{2}}} = \frac{El[(2G_S{}^2 H_{bias} - G_{AS})H]}{\left[\left(\frac{E^2}{nwt}\frac{l}{\Delta f} + \frac{4kTl}{nwte}\right)\Delta f\right]^{\frac{1}{2}}} \quad (3)$$

where I_{in} is the input current, V is input voltage, L (l) is the spacing of the current (voltage) leads, α is the dimensionless Hooge parameter, e is the electron charge, f is the operating frequency, Δf is the detection bandwidth, k is Boltzman's constant, T is temperature in Kelvin, R_{out} is the two terminal resistance between the voltage probes including the contact resistance at the interface

T (K)	Hall Probe[b] GaAs/AlGaAs 1 m 1 m 25nm	EMR Probe[c] InSb/AlInSb 1 m 1 m 25nm	EMR Probe[c] InSb/AlInSb 35nm 30nm 25nm	EMR Probe[d] InAs 1 m 1 m 25nm	EMR Probe[d] InAs 35nm 30nm 25nm
300	4 10^{6} [4 10^{6}] f0.016g	2:1 10^{8} [7:4 10^{5}] f0.300g	4:1 10^{6} [2:2 10^{6}] f0.009g	1:2 10^{8} [1:3 10^{4}] f0. 512g	2:4 10^{6} [3:8 10^{6}] f0.015g
77	3 10^{8} [6 10^{5}] f0.24g	NA	NA	1:3 10^{9e} [2:0 10^{4}] f0.8g	2:6 10^{7} [5:9 10^{6}] f0.024g
4	1 10^{8e} [6 10^{5}] f0.24g	NA	NA	9:8 10^{12e} [5:3 10^{4}] f2.1g	1:9 10^{9e} [1:6 10^{5}] f0.064g

TABLE I: A comparison of the NEF ($THz^{1=2}$), maximum bias current (A) [shown in square brackets] and self-field[a] (mT) {shown in curly brackets} of Hall and EMR probes at three different temperatures. [a] At a distance 50nm from the center of the active region of the sensor. [b] Data taken directly from or computed from ref. 2. Oral et al. (ref. 4) report a Hall probe with 250 nm lateral spatial resolution and a field sensitivity of 3 10^{7} $THz^{1=2}$ at 77 K but details were not available to allow inclusion of this in Table I. [c] n_{2D} = 5 10^{11} cm^{2}, $_{300}$ = 2:3 10^{4} cm^{2}/Vs, E_{max} = 400 V/cm, H_{bias} = 0. Assumed voltage and current contacts with negligible contact resistance. [d] The temperature dependence of the mobility was computed using the Caughey & Thomas formula. Parameters for the surface accumulation layer: n_{2D} = 1 10^{12} cm^{2}, $_{300}$ = 2 10^{4} cm^{2}/Vs, E_{max} = 400 V/cm. Assumed dR^{eff}/dH scales with ^{2}. [e] Intrinsic value. Preamp noise limit at 300K is 3 10^{8}.

between the voltage probes and the device, E = V=L is the bias electric field, l is the voltage probe spacing, n is the carrier (electron) density, wt is the crossectional area for bias current flow and the other variables in Eq. (3) have been previously defined. The first term in each of the denominator brackets is the 1=f noise while the second term is the thermal noise. By equating these two terms we can deduce the crossover frequency $f_c = E^2 (e=4kT)$. For $f \ll f_c$ thermal noise dominates and the SNR is frequency independent while for $f \gg f_c$ 1=f noise dominates and the SNR is independent of the bias field.

It is useful at this point to estimate the crossover frequency for a nanoscopic EMR sensor. The relevant parameters are 10^{8}, 2:3 10^{4} cm^{2}/Vs, E 4 10^{6} V/cm (see discussion below) in which case f_c 400Hz at 300K and f_c 30KHz at 4K. Clearly, it is desirable to operate the EMR sensor at sufficiently high frequency to be in the thermal noise limited region. Moreover, since optimizing the controllable parameters in Eq. (3) to achieve minimal thermal noise collaterally minimizes the 1/f noise we focus here on the former. Note that l,w and t are set by the required three-dimensional resolution, and H is set by the available signal so these parameters are deemed uncontrollable.

In the thermal noise and 1=f noise regimes the SNR increases as $n^{5=2}$ and n^{2}, respectively. Therefore, it is advantageous to maximize these products. Since for n(T) > n_c(T) mobility decreases[27] with increasing n where n_c(T) is a critical concentration the SEMRPM will be designed to operate at or near n_c(T). For room temperature probes, n_c(300 K) 5 10^{17} cm^{3} for both InSb and InAs.[28]

The SEMRPM performance can best be evaluated by comparing it to comparable probes based on the Hall effect in GaAs/AlGaAs heterostructures since the two sensor types will share many similarities. The figure of merit appropriate to such a comparison is the noise equivalent field (NEF)[29] that is obtained from Eq. (3) by setting $SNR(f) = 1$ and solving for the resultant value of $H = \sqrt{f}$. The thermal noise limit NEF figures of an EMR probe fabricated from an InSb quantum well structure and from InAs bulk thin films are compared to corresponding values of a Hall probe in Table I. Also shown in that table are the self-field of the probe (e.g. the field near the probe produced by its own bias current) at a distance of 50 nm from the center of its active region. To facilitate direct comparison, the performance of each probe is calculated for a standard set of dimensions 1 m 1 m 25 nm using reported/measured maximal current densities. For the Hall probe, key data is taken directly from ref. 2 and references therein. For the InSb probe, the current sensitivity of 585 /T is taken from the data of Fig. 3. For InAs the current sensitivity is assumed to scale as ^{2} and the temperature dependence of is obtained from the Caughey – Thomas formula.[30]

As can be seen from Table I, the EMR probe offers significant potential advantages over the Hall probe in sensitivity, spatial resolution and self-field strength. Moreover, like the Hall probe, the EMR probe should be capable of very wide band width operation leading to attractive signal to noise ratios. While the data of Table I appears to favor the InAs system over the InSb system for EMR probe applications at all temperatures, the latter appears to offer greater opportunity for developing high mobility materials for room temperature applications. Therefore, it is proposed that both systems be developed in parallel in order to insure the development of a superior EMR probe.

E. SEMRPM Fabrication and Construction

Wafers will be fabricated into the mesoscopic structures appropriate to the SEMRPM application and instrumentation. The fabrication process which has been described in detail elsewhere,[10] will involve application of a Si_3N_4 overcoat to the material wafer, state of the art e-beam lithography using calixarene resist, reactive ion etching and suspended mask metallization. The EMR probe will be coupled to the piezoelectric scanner tube of a commercial low temperature scanning tunneling microscope housed in an superconducting solenoid capable of 1.5K – 325K operation at fields up to 10T. The design is similar to one developed by Bending and coworkers[2] that is popular for SHPM's and allows for convenient simultaneous acquisition of both the (standard DC[2] or AC[31]) EMR probe and the STM signals thus providing both topographic and magnetic images.

IV. SUMMARY AND CONCLUSIONS

We have shown that the SEMRPM, once constructed according to the design criteria described above, should significantly advance the state of the art of magnetic nanoprobe technology. A program has been undertaken by the author to fabricate the SEMRPM and to employ it to address several problems in basic and applied science. Results derived from this program will be reported in the near future.

V. ACKNOWLEDGMENTS

Useful discussions with A.C.H. Rowe, D.R. Hines and L. Cohen are gratefully acknowledged. This work was supported by the NSF under grant # ECS-0329347.

Electronic address: solin@wustl.edu

1. A. Companieh, R. Eaton, R. S. Indeck, and M. Moser, IEEE Trans. on Magn., (2001).
2. S.J. Bending, Advances in Physics 48, No. 4 (1999).
3. G.D. Howells, A. Oral, S.J. Bending, S.R. Andrews, P.T. Squire, P. Rice, A. de Lozanne, J.A.C. Bland, I. Kaya and M. Henini, J. Magnetism and Mag. Matls. 917, 196 (1999).
4. Nonmagnetic system such as quantum wire with current.
5. A. Volodin, K. Temst, C. Van Haesendonck and Y. Bruynseraede, Appl. Phys. Lett. 73, 1134 (1998).
6. A. Oral, S.J. Bendin and M. Henini, Appl. Phys. Lett. 69, 1324 (1996).
7. A Crisan, A Pross, R G Humphreys and S Bending, Supercond. Sci. Technol. 16, 695 (2003).
8. V. Umansky, R. de-Picciotto, and M. Heiblum, Appl. Phys. Lett. 71, 683 (1997)
9. S.A. Solin, Tineke Thio, D.R. Hines and J.J. Heremans, Science 289, 1530 (2000).
10. S.A. Solin, D.R. Hines, J.S. Tsai, Yu.A. Pashkin, S.J. Chung, N. Goel and M.B. Santos, Appl. Phys. Letters 80, 4012 (2002).
11. R.S. Popovic, Hall effect devices, (Adam Hilger, Bristol, 1991).
12. Tineke Thio and S.A. Solin, Appl. Phys. Lett., 72, 3497 (1998).
13. W.F. Egelhoff, Jr., et al., J. Appl. Phys. 78, 273 (1995).
14. C. Mitra, P. Raychaudhuri, G. Kobernik,, K. Dorr, K.H. Muller, L. Schultzand and R. Pinto, Appl. Phys. Lett. 79, 2408 (2001)
15. S. Jin, M. McCormack, T.H. Tiefel and R. Ramesh, J. Appl. Phys. 76, 6929 (1994).
16. S.A. Solin, D.R. Hines, J.S. Tsai, Yu.A. Pashkin, S.J. Chung, N. Goel and M.B. Santos, Appl. Phys. Letters 80, 4012 (2002).
17. J. Moussa, L.R. Ram-Mohan, J. Sullivan, T. Zhou, D.R. Hines, and S.A. Solin, Phys Rev. B 64, 184410 (2001).
18. T. Zhou, D.R. Hines and S.A. Solin, Appl. Phys. Lett. 78, 667 (2001).
19. Yu.A. Pashkin, Y. Nakamura, and J.S. Tsai, Appl. Phys. Lett. 76, 2256 (2000).
20. S.A. Solin, Tineke Thio, J.W. Bennett, and D.R. Hines M. Kawano, N. Oda, and M. Sano, Appl. Phys. Lett. 69, 4105 (1996).
21. S. Sze, Physics of Semiconductor Devices, (Wiley, New York, 1968).
22. Ref to grundler's work in InAs Microscopic structures.
23. P.D. Wang et al., Semiconductor Science & Tech. 7, 767 (1992).
24. S.D. Parker, et al., Semicond. Sci. Technology 4, (1989) 663.
25. A.C.H. Rowe, C. Gatzke, R.A. Stradling and S.A. Solin, Appl. Phys. Lett. 76, 1902 (2000)
26. M.B. Weissman, Rev. Mod. Phys. 60, 537 (1988).
27. K. Seeger, Semiconductor Physics, (Springer-Verlag, Berlin, 1985, 3rd edition)
28. O. Madulung, Ed., Semiconductors: Group IV Elements and III–V Compounds, (Springer-Verlag, New York, 1991).
29. M.N. Deeter, G.W. Day; T.J. Beahn; M. Manheimer, Elec. Lett. 29 933 (1993).
30. D. Caughey and R. Thomas, Proc. IEEE, 52, 2192 (1967).
31. M. Marchevsky, M.J. Higgins and S. Bhattacharya, Nature 409, 591 (2001).